

Parametric Reduced Order Models for the Generalized Kuramoto–Sivashinsky Equations

Md Rezwan Bin Mizan ^{*} Maxim Olshanskii [†] Ilya Timofeyev [‡]

Abstract

The paper studies parametric Reduced Order Models (ROMs) for the Kuramoto–Sivashinsky (KS) and generalized Kuramoto–Sivashinsky (gKS) equations. We consider several POD and POD-DEIM projection ROMs with various strategies for parameter sampling and snapshot collection. The aim is to identify an approach for constructing a ROM that is efficient across a range of parameters, encompassing several regimes exhibited by the KS and gKS solutions: weakly chaotic, transitional, and quasi-periodic dynamics. We describe such an approach and demonstrate that it is essential to develop ROMs that adequately represent the short-time transient behavior of the gKS model.

1 Introduction

Reduced-order modeling (ROM) of systems exhibiting chaotic (turbulent) and more deterministic (laminar) behavior has been an active area of research for several decades. ROMs have been successfully applied to numerically solve various mathematical models of such systems, often formulated in terms of partial differential equations (PDEs). A major ongoing challenge is developing ROMs that remain both effective and efficient across a range of parameter values upon which the system may depend, particularly when the solution behavior transitions from chaotic to more deterministic depending on these parameters. Solving such parametric systems is a common need in fields like uncertainty quantification and inverse modeling.

The development of ROMs for parametric fluid systems has already been addressed in the literature; see, e.g., [26, 40, 22, 18, 42, 19] for the recent work on the subject. These studies primarily consider cases where the flow regime does not change under the allowed variation of parameters, remaining either laminar, transitional, or turbulent. However, there are situations, such as in shape design, where the flow’s statistical behavior changes dramatically depending on the parameter values. In these cases, ROMs that perform well for laminar flows may fail to represent turbulent solutions, and vice versa.

To gain insight into the behavior of projection-based ROMs (such as POD-ROMs) under these conditions and to provide practical recommendations, this paper focuses on a prototypical model: the generalized Kuramoto–Sivashinsky (gKS) equations. The solutions to these equations exhibit various regimes, ranging from spatio-temporal chaos to quasi-periodic behavior, with the regime largely determined by the value of a critical parameter.

The development of ROMs for the KS and gKS equations has already been addressed in the literature. Existing approaches include stochastic reduced models [50, 44, 31], POD-ROMs [30, 56, 45], and neural network-based ROMs [37, 1]. However, these studies have primarily focused on recovering statistics of interest for either chaotic or deterministic solutions of the equations through reduced modeling.

The paper focuses on projection-based reduced-order models (ROMs), which construct surrogate models by projecting a high-fidelity system onto a low-dimensional, problem-dependent vector space [5]. Prominent examples of such ROMs for dynamical systems include proper orthogonal decomposition (POD) ROMs [32, 46] and its variants, such as POD-DEIM [8] and balanced POD [43], along with PGD-ROMs [9, 10]. These

^{*}Dept. of Mathematics, University of Houston, Houston, TX 77204, mbinmiza@cougarnet.uh.edu

[†]Dept. of Mathematics, University of Houston, Houston, TX 77204, maolshanskiy@uh.edu

[‡]Dept. of Mathematics, University of Houston, Houston, TX 77204, itimofey@cougarnet.uh.edu

methods derive the projection basis by leveraging information from high-fidelity solutions sampled at specific time instances and/or parameter values, commonly referred to as solution snapshots. However, constructing a general low-dimensional space that remains accurate across a wide range of parameters and over long time horizons can be highly challenging, if not infeasible. While such a space may effectively capture the training data, it often lacks predictive accuracy beyond the reference simulations.

Several approaches have been proposed to address this limitation. Partitioning strategies, introduced in [16, 15, 3], divide the parameter domain and assign local reduced-order bases to each subdomain offline. In [2, 49], the authors suggested adapting precomputed reduced-order spaces by interpolating them for out-of-sample parameters along geodesics on the Grassmann manifold. Another approach, which utilizes the inherent tensor structure of the space-time-parameter domain to build parameter-specific local reduced spaces, was introduced in [34, 35]. While these techniques have shown varying degrees of success in systems with smooth parameter dependencies and relatively simple solution manifolds, it is still a challenge to extend the methodology for a parametric dynamical system exhibiting multiple regimes within the given parameter range. In this paper, we take a step in addressing this challenge and investigate the feasibility of several strategies for building projection based ROMs (POD-ROM and POD-DEIM-ROM) for the model example of the generalized Kuramoto-Sivashinsky equation.

The paper investigates several single-parameter and multi-parameter training strategies for training a reduced-order model (ROM). We examine how the selection of the training set of parameters and initial conditions affects the ROM's ability to predict solutions across various regimes exhibited by the KS and gKS equations: weakly chaotic, transitional, and quasi-periodic dynamics. We will show that efficient prediction of solutions beyond the set of parameters and initial conditions used for training requires including additional snapshots that capture chaotic or short-time transient behaviors of the gKS model. Additionally, the paper argues that conventional error metrics, such as the difference between FOM and ROM solutions measured in various norms, may not always be suitable for assessing ROM performance—not only in turbulent regimes but also for transitional solutions that exhibit the formation of persistent patterns. In addition, for turbulent regimes, we examine whether ROMs reproduce the statistical behavior of solutions. To this end, we compare the power spectra computed from FOM and ROM simulations.

The remainder of the paper is organized as follows. Sections 2 and 3 review the KS and gKS equations and the parametric POD-ROM, respectively. Section 4, the core of the paper, introduces our training strategies and the metrics used to assess ROM quality. Depending on the value of the problem parameter, our study covers three solution regimes: the chaotic regime (Section 4.1.2), the transient regime with persistent pattern formation (Section 4.1.3), and the laminar regime (Section 4.1.4). Section 4.2 examines the performance of the DEIM hyper-reduction technique for handling nonlinear terms in the equations. Finally, several conclusions are presented in Section 5.

2 KS and gKS equations

Kuramoto-Sivashinsky (KS) equation [29, 47] has become a classical model for studies of spatio-temporal chaos. The generalized Kuramoto-Sivashinsky (gKS) equation in 1D has the following form

$$\frac{\partial u}{\partial t} + \frac{1}{2} \frac{\partial u^2}{\partial x} + \frac{\partial^2 u}{\partial x^2} + \gamma \frac{\partial^3 u}{\partial x^3} + \frac{\partial^4 u}{\partial x^4} = 0 \quad (1)$$

usually supplemented with periodic boundary conditions $u(0, t) = u(L, t)$. The KS equation is a particular case of the gKS with $\gamma = 0$. In (1), L plays the role of the bifurcation parameter which determines the number of linearly unstable Fourier modes $S_{unst} = \lfloor \frac{L}{2\pi} \rfloor$, where $\lfloor \cdot \rfloor$ denotes the lowest integer. The most unstable wavenumber is given by $M_{unst} = \frac{L}{2\sqrt{2\pi}}$.

The KS equation has been the subject of an extensive investigation. In particular, it was demonstrated that the KS model has a finite-dimensional attractor and, thus, is equivalent to a finite-dimensional dynamical system [12, 20, 39] (see [51] for an overview). Moreover, it can be shown that the attractor is an inertial manifold [24, 11, 52]. Many other analytical and numerical studies have been performed (e.g. [28, 23, 48, 38]).

The dynamics of the gKS equation also has been studied extensively (e.g. [27, 36, 25, 4, 6, 17, 13, 54, 14, 53, 41, 7]). It has been demonstrated that parameter γ has a strong influence on the dynamics of the gKS equation. For smaller values of γ near zero, the system exhibits spatio-temporal chaos, similar to the KS equation. As γ increases, the system exhibits a transition towards less chaotic or even non-chaotic dynamics (see [21] for a detailed numerical study). In the limit $\gamma \rightarrow \infty$ the gKS equation is equivalent to the integrable Korteweg–deVries (KdV) equation (e.g. [54]).

3 Parametric POD–DEIM–ROM

For the space discretization of (1) we use a uniform grid on $[0, L]$ and apply a finite-difference discretization where nonlinear fluxes $F(u) = -u^2/2$ are discretized explicitly using $F_{i+1/2} = -(u_i^2 + u_i u_{i+1} + u_{i+1}^2)/6$ and linear terms are discretized implicitly. This discretization of the nonlinear term was used previously in [55, 33]. The resulting system of ODEs takes the form of the parameterized dynamical systems: for a given γ from the parameter domain $\mathcal{G} = [0, \Gamma]$ find $\mathbf{u} = \mathbf{u}(t, \gamma) : [0, T] \rightarrow \mathbb{R}^M$ solving

$$\mathbf{u}_t = \mathbf{A}(\gamma)\mathbf{u} + \mathbf{f}(\mathbf{u}), \quad t \in (0, T), \quad \text{and } \mathbf{u}|_{t=0} = \mathbf{u}_0. \quad (2)$$

Here $\mathbf{A}(\gamma)$ is an $M \times M$ matrix corresponding to the linear space derivatives in (1) and $\mathbf{f} : \mathbb{R}^M \rightarrow \mathbb{R}^M$ stands for the discrete nonlinear term; \mathbf{u}_0 is an initial value projected on the grid.

To formulate a POD–DEIM ROM for (2), consider a training set of K parameters sampled from the parameter domain, $\hat{\mathcal{G}} := \{\hat{\gamma}_1, \dots, \hat{\gamma}_K\} \subset \mathcal{G}$. Hereafter we use hats to denote parameters from the training set $\hat{\mathcal{G}}$. At the first, offline stage of POD–DEIM, one computes through the full-order numerical simulations a collection of solution snapshots

$$\phi_j(\hat{\gamma}_k) = \mathbf{u}(t_j, \hat{\gamma}_k) \in \mathbb{R}^M, \quad j = 1, \dots, N, \quad k = 1, \dots, K, \quad (3)$$

and non-linear term snapshots

$$\psi_j(\hat{\gamma}_k) = \mathbf{f}(\mathbf{u}(t_j, \hat{\gamma}_k)) \in \mathbb{R}^M, \quad j = 1, \dots, N, \quad k = 1, \dots, K, \quad (4)$$

further referred to as \mathbf{u} - and \mathbf{f} -snapshots, respectively, at times $0 \leq t_1, \dots, t_N \leq T$, and for $\hat{\gamma}_k$ from the training set $\hat{\mathcal{G}}$. For a desired reduced space dimension $n \ll M$, one computes the reduced space basis $\{\mathbf{u}_i^{\text{pod}}\}_{i=1}^n \subset \mathbb{R}^M$, referred to as the *POD basis*, such that the projection subspace $\text{span}\{\mathbf{u}_1^{\text{pod}}, \dots, \mathbf{u}_n^{\text{pod}}\}$ approximates the space spanned by all \mathbf{u} -snapshots in the best possible way. This is achieved by assembling the matrix of all \mathbf{u} -snapshots

$$\Phi_{\text{pod}} = [\phi_1(\gamma_1), \dots, \phi_N(\gamma_1), \dots, \phi_1(\gamma_K), \dots, \phi_N(\gamma_K)] \in \mathbb{R}^{M \times NK} \quad (5)$$

and computing its SVD. Then, the POD reduced basis $\mathbf{u}_i^{\text{pod}}, i = 1, \dots, n$, consists of the first n left singular vectors of Φ_{pod} .

Consider how the $M \times n$ matrix $\mathbf{U}_{\text{pod}} = [\mathbf{u}_1^{\text{pod}}, \dots, \mathbf{u}_n^{\text{pod}}]$. At the second, online stage, the POD–ROM solution \mathbf{u}^{rom} is found through its vector of coordinates $\boldsymbol{\beta}$ in the space $\text{range}(\mathbf{U}_{\text{pod}})$, i.e., $\mathbf{u}^{\text{rom}} = \mathbf{U}_{\text{pod}}\boldsymbol{\beta}$, which solve the projected system

$$\boldsymbol{\beta}_t = \mathbf{U}_{\text{pod}}^T \mathbf{A}(\gamma) \mathbf{U}_{\text{pod}} \boldsymbol{\beta} + \mathbf{U}_{\text{pod}}^T \mathbf{f}(\mathbf{U}_{\text{pod}} \boldsymbol{\beta}), \quad t \in (0, T), \quad \text{and } \boldsymbol{\beta}|_{t=0} = \mathbf{U}_{\text{pod}}^T \mathbf{u}_0. \quad (6)$$

While the projected matrix $\mathbf{U}_{\text{pod}}^T \mathbf{A}_\gamma \mathbf{U}_{\text{pod}}$ can be pre-computed during the offline stage, to efficiently evaluate the nonlinear term in (6) during the online stage, we apply the discrete empirical interpolation method (DEIM) [8]. In this widely-used hyper-reduction technique, the nonlinear term is approximated within a lower-dimensional subspace of the space spanned by all \mathbf{f} -snapshots. To define the orthogonal basis $\{\mathbf{y}_i^{\text{pod}}\}_{i=1}^n \subset \mathbb{R}^M$ for this subspace, one takes the first n left singular vector of the matrix:

$$\Psi_{\text{pod}} = [\psi_1(\gamma_1), \dots, \psi_N(\gamma_1), \dots, \psi_1(\gamma_K), \dots, \psi_N(\gamma_K)] \in \mathbb{R}^{M \times NK}, \quad (7)$$

consisting of all pre-computed \mathbf{f} -snapshots. These n first left singular vectors of (7) form the matrix $\mathbf{Y}_{\text{pod}} = [\mathbf{y}_1^{\text{pod}}, \dots, \mathbf{y}_n^{\text{pod}}]$. Then, DEIM approximates the nonlinear term of (2) via

$$\mathbf{f}(\mathbf{u}) \approx \mathbf{Y}_{\text{pod}}(\mathbf{P}^T \mathbf{Y}_{\text{pod}})^{-1} \mathbf{P}^T \mathbf{f}(\mathbf{u}), \quad (8)$$

where the ‘selection’ matrix is defined as:

$$\mathbf{P} := [\mathbf{e}_{\eta_1}, \dots, \mathbf{e}_{\eta_n}] \in \mathbb{R}^{M \times n}, \quad (9)$$

This matrix, \mathbf{P} , is constructed so that for any $\mathbf{f} \in \mathbb{R}^M$, the vector $\mathbf{P}^T \mathbf{f}$ contains n entries selected from \mathbf{f} with indices $\boldsymbol{\eta} = [\eta_1, \dots, \eta_n]^T \in \mathbb{R}^n$. DEIM determines $\boldsymbol{\eta}$ entirely based on the information within \mathbf{Y}_{pod} using a greedy algorithm; we refer to [8] for further details.

The singular values of Φ_{pod} and Ψ_{pod} provide information about the representation power of the ROMs subspaces $\text{span}\{\mathbf{u}_1^{\text{pod}}, \dots, \mathbf{u}_n^{\text{pod}}\}$ and $\text{span}\{\mathbf{y}_1^{\text{pod}}, \dots, \mathbf{y}_n^{\text{pod}}\}$, respectively. In particular, the following estimate follows from the Eckart–Young–Mirsky theorem:

$$\sum_{k=1}^K \sum_{i=1}^N \left\| \phi_i(\gamma_k) - \sum_{j=1}^n \langle \phi_i(\gamma_k), \mathbf{u}_j^{\text{pod}} \rangle \mathbf{u}_j^{\text{pod}} \right\|_{\ell^2}^2 \leq \sum_{j=n+1}^{NK} \sigma_j^2(\Phi_{\text{pod}}), \quad (10)$$

for representation of the solution states, and similarly for $\mathbf{y}_j^{\text{pod}}$ and \mathbf{f} -snapshots $\psi_i(\gamma_k)$. Therefore, to determine the dimension of the reduced space, we take such minimal n that

$$\sum_{j=n+1}^{NK} \sigma_j^2(\Phi_{\text{pod}}) \leq \varepsilon \|\Phi_{\text{pod}}\|_F^2$$

with the threshold parameter ε .

Summarizing, the POD–DEIM ROM of (2) takes the form

$$\boldsymbol{\beta}_t = \mathbf{U}_{\text{pod}}^T \mathbf{A}(\gamma) \mathbf{U}_{\text{pod}} \boldsymbol{\beta} + (\mathbf{U}_{\text{pod}}^T \mathbf{Y}_{\text{pod}})(\mathbf{P}^T \mathbf{Y}_{\text{pod}})^{-1} \mathbf{P}^T \mathbf{f}(\mathbf{U}_{\text{pod}} \boldsymbol{\beta}), \quad t \in (0, T), \quad (11)$$

with the initial condition $\boldsymbol{\beta}|_{t=0} = \mathbf{U}_{\text{pod}}^T \mathbf{u}_0$, for $\boldsymbol{\beta}(t) : [0, T] \rightarrow \mathbb{R}^n$ so that $\mathbf{u}(t)$ is approximated by $\mathbf{u}^{\text{rom}}(t) : [0, T] \rightarrow \text{span}\{\mathbf{u}_1^{\text{pod}}, \dots, \mathbf{u}_n^{\text{pod}}\}$, where $\mathbf{u}^{\text{rom}}(t) = \mathbf{U}_{\text{pod}} \boldsymbol{\beta}(t)$.

Remark. We also consider the case where the initial condition $u_0(x, \vec{\alpha})$ in (2) is parametrized by a parameter vector $\vec{\alpha}$ from a parameter domain in \mathbb{R}^J . In this case, the parameter domain is sampled with W trial values for each γ_i , where $i = 1, \dots, K$. Therefore, the matrices Φ_{pod} and Ψ_{pod} from (5) and (7) are $M \times (NKW)$ matrices. We distinguish between the sampling of parameters γ and $\vec{\alpha}$, as these parameters play very different roles in the system dynamics. For each fixed $\vec{\alpha}$, the set of collected snapshots will be referred to as a ‘trajectory’.

4 Numerical Results and Analysis

In this section, we present our numerical results on the performance of ROMs for the KS and gKS equations. Specifically, we focus on constructing ROMs with high predictive utility across a range of parameter values γ . This task is particularly challenging because the behavior of the gKS equation changes drastically as γ increases (see, e.g., [21]). Notably, the chaotic regime is relatively narrow, occurring approximately within $\gamma \in [0, 0.15]$. We demonstrate that even for larger γ , ROMs built with a sufficient number of chaotic or ‘‘transient’’ (non-chaotic regime) snapshots significantly outperform those constructed from purely non-chaotic time series. To this end, we analyze ROMs constructed from datasets specifically designed to emphasize either the chaotic (or transient) regime or the more deterministic behavior.

Parameters and Initial Conditions. We use the following parameters in simulations of the KS and gKS equations. The number of spatial points is $M = 256$, domain size $L = 60$ (except for Figure 1 and corresponding simulations), time-step $\delta t = 0.001$, the total number of snapshots for constructing ROMs is $N^* = 20,000$, time-step for collecting snapshots $\Delta t = 0.5$. The domain size $L = 60$ corresponds to 18 unstable wavenumbers in Fourier space, and the most unstable wavenumber is 7. For all simulations, initial conditions are generated as

$$u(x, 0) = \sum_{j=1}^J A_j \cos\left(\frac{2\pi j x}{L} + \phi_j\right), \quad (12)$$

where $A_j \sim 0.1 \times \text{Unif}[-1, 1]$, $\phi_j \sim \text{Unif}[0, 2\pi]$. To build our ROMs, we utilize $J = 8$, while testing the ROMs' performance and robustness, we employ a broader range of values $J = 3, 8, 22$.

Selecting the Reduced dimension. Singular Value Decomposition (SVD) is used to identify the minimum number of singular values necessary to accurately represent the data. First, we define *cumulative sum of singular values* $S_i = \sum_{j \geq i} \sigma_j$ and *cumulative variance ratio* $C_i = S_i/S_1$. Then we define the *optimal reduced dimension* as $r = \min\{i : C_i < V\}$, where V is a preselected threshold. In this paper, we use $V = 10^{-2}$, i.e. our ROMs bases accumulate 99% of the energy).

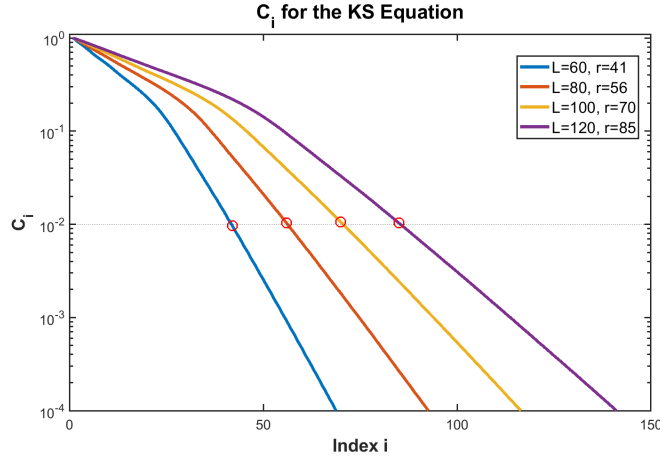


Figure 1: Simulations of the KS equation. Cumulative variance ratio, C_i , for different values of L and the corresponding optimal reduced dimension. The optimal reduced dimension is selected when C_i becomes less than 10^{-2} .

To analyze the effect of the spatial domain length L on reduced dimension selection, cumulative sums of singular values are plotted for four values of L in Figure 1. The figure demonstrates that larger L values require more singular vectors to adequately capture the system's behavior. This reveals a linear relationship between L and the number of modes necessary to construct ROMs with the same threshold V as L increases. Since the number of unstable wavenumbers scales linearly with L , the KS equation exhibits greater complexity for larger L , requiring a higher rank to effectively capture the dynamics of the KS and gKS models.

4.1 Comparing Performance of Different ROMs

From now on, we consider $L = 60$. In our study, we construct the reduced basis for ROMs using $N^* = 20,000$ snapshots of the FOM solution. We consider several approaches for sampling these snapshots from numerical solutions. In particular, we analyze several ROMs where Φ_{pod} is constructed using snapshots for a single

value of γ , as well as ROMs where Φ_{pod} is constructed using a combination of snapshots for multiple values of γ . In all cases, the total number of snapshots is N^* , and the sampling time-step is $\Delta t = t_{j+1} - t_j = 0.5$.

All ROMs discussed in this paper are constructed using $V = 10^{-2}$ as a threshold. The corresponding ranks vary slightly for different approaches but fall within the range $r \in [41, 47]$.

Next, we compare and contrast the following three approaches:

- **Single trajectory sampling for $\gamma = 0$:** Sample snapshots from a single trajectory for $\gamma = 0$. The total simulation time is $T_s = 10,000$, corresponding to $N = N^*$, $K = 1$, and $W = 1$. The dimension of this ROM is $r = 41$.
- **Multiple trajectory sampling for $\gamma = 5$:** Sample snapshots from W trajectories generated using different initial conditions for a single $\gamma = 5$ ($K = 1$). When W increases, the total number of collected snapshots remains fixed at N^* . Consequently, trajectories become shorter, and a larger percentage of snapshots are sampled from the chaotic (or transient) regime. Specifically, we consider $W = 250, 100$, and 25 , with the total number of snapshots from a single trajectory being N^*/W . The resulting ranks are 46, 47, and 47, respectively.
- **Multi-parameter sampling for γ :** Sample snapshots from trajectories generated using multiple values of γ . We use $W = 1$ and $K = 5$ different values of γ , with $N = N^*/K = 4,000$ snapshots sampled for each value. Although the number of parameters is fixed at $K = 5$, we consider four different parameter domains $\hat{\mathcal{G}}$ for sampling:

- (i) $\hat{\mathcal{G}}_1 = \{3, 4, 5, 7, 10\}$
- (ii) $\hat{\mathcal{G}}_2 = \{0, 4, 5, 7, 10\}$
- (iii) $\hat{\mathcal{G}}_3 = \{0, 0.3, 1, 5, 10\}$
- (iv) $\hat{\mathcal{G}}_4 = \{0, 0.2, 0.5, 0.7, 0.9\}$

The corresponding ranks are 44, 43, 41, and 41, respectively.

Recall that smaller values of γ correspond to chaotic (or transient) regimes. Therefore, $\hat{\mathcal{G}}_1$ includes very few snapshots from the chaotic regime, while $\hat{\mathcal{G}}_4$ includes many snapshots from the chaotic regime. We observe that the performance of the ROM improves as more chaotic snapshots are included in Φ_{pod} .

Performance assessment: To gauge the performance of ROMs, we will focus on several statistics such as (i) Prediction time (measures the short-term prediction capability of the ROM); (ii) Power spectra (measures the statistical properties of chaotic solutions); (iii) Persistent patterns (assesses the prediction of long-term solution behavior).

4.1.1 Averaged Prediction Time.

First, we evaluate the performance of different reduced order models by comparing the prediction accuracy for several randomly chosen initial conditions. For this purpose, we define the prediction time of the ROM for a given initial condition as

$$T_{\text{rom}}(u_0) = \arg \max_{t \in [0, T]} \left\{ t : \sup_{t' \in [0, t]} \frac{\|u^{\text{rom}}(t') - u^{\text{fom}}(t')\|_{L^2(0, L)}}{\|u^{\text{fom}}(t')\|_{L^2(0, L)}} \leq 10^{-1} \right\}, \quad (13)$$

where u^{fom} solves (2).

In particular, we consider initial conditions given by (12) with three different values of $J = 3, 8, 22$. Averaged prediction times for two single-parameter ROMs are depicted in Figure 2 and for multi-parameters ROMs in Figure 3. We considered three random initial conditions for each J and γ and calculated the prediction time according to (13). The averaged prediction time is then computed by averaging over the three initial conditions.

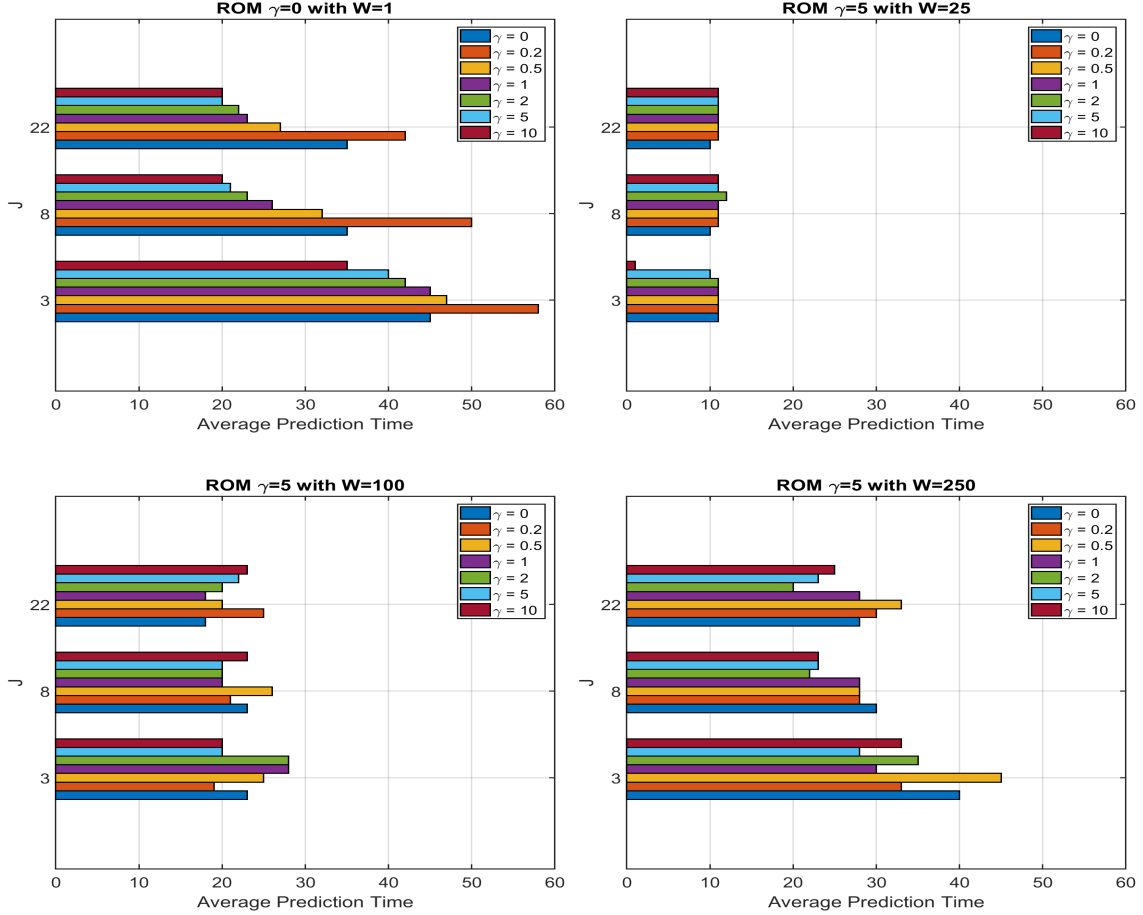


Figure 2: Averaged prediction times for trajectories of the gKS equation with different values of γ using ROMs constructed using gKS data with a single value of γ . Upper left - ROM is constructed from simulations with $\gamma = 0$ and $W = 1$. Upper right, bottom left, bottom right - ROM is constructed from simulations with $\gamma = 5$ with $W = 25, 100, 250$, respectively. We consider 3 sets of different initial conditions with $J = 3, 8, 22$, where J is the number of non-zero Fourier wavenumbers at time $t = 0$ (see eq. (12)).

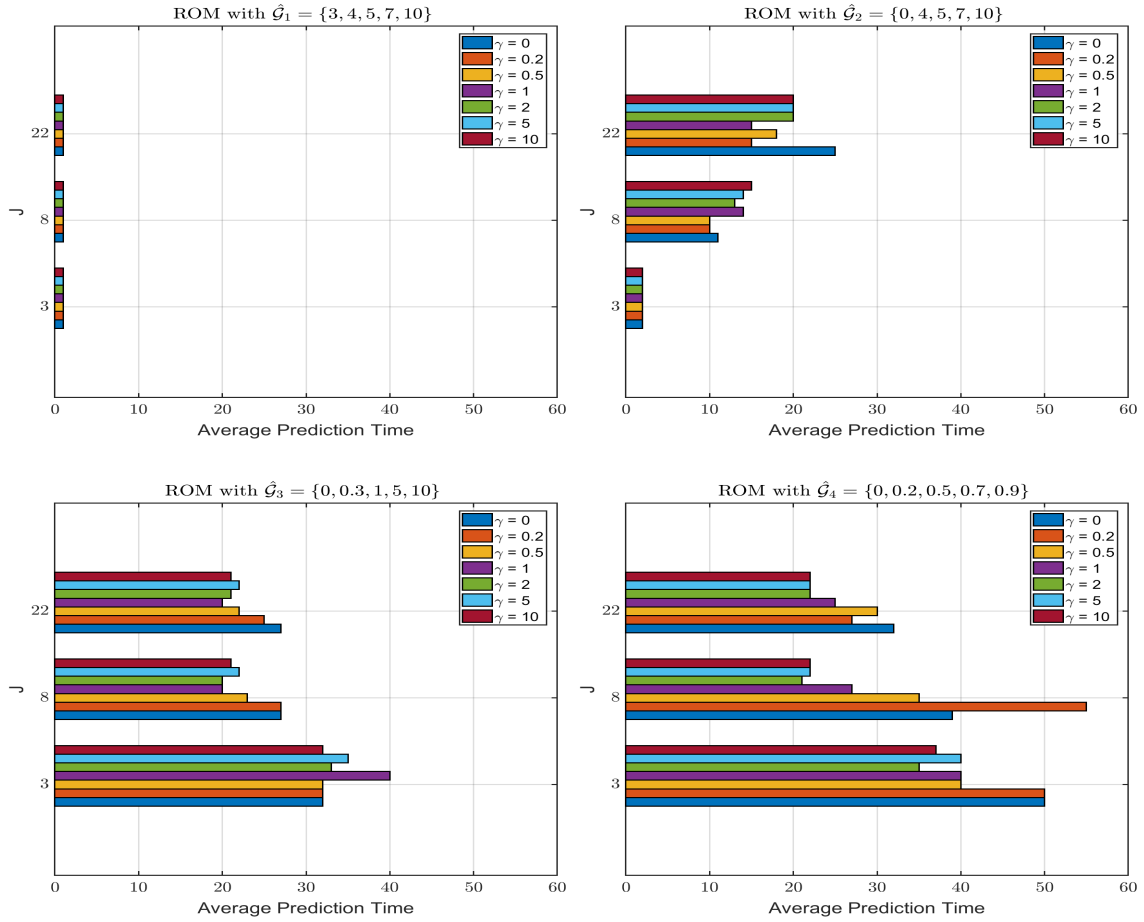


Figure 3: Averaged prediction times for trajectories of the gKS equation with different values of γ using multi-valued ROMs constructed using gKS data with $K = 5$ values of γ and $W = 1$. For each γ , we consider 3 sets of different initial conditions with $J = 3, 8, 22$, where J is the number of non-zero Fourier wavenumbers at time $t = 0$ (see eq. (12)).

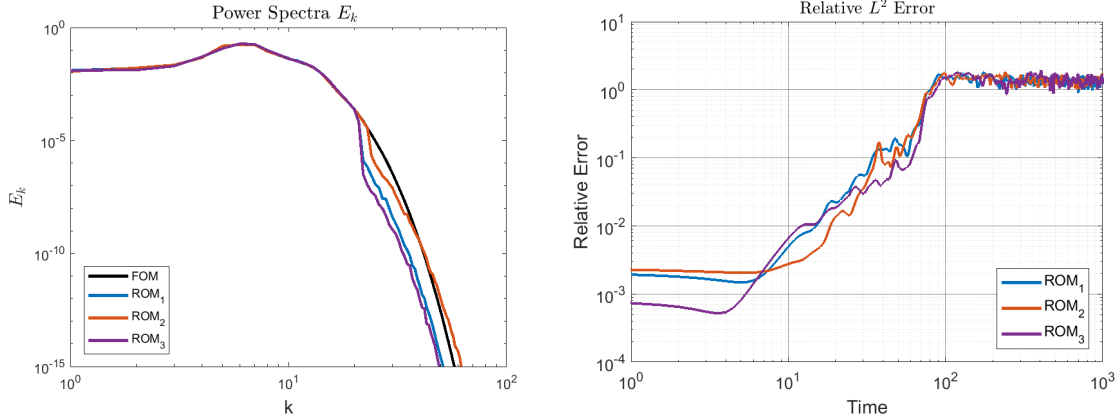


Figure 4: Power Spectra (left) and a typical L^2 error for a single trajectory (right) for $\gamma = 0.1$.

We observe that the ROM constructed from $\gamma = 0$ data has the best performance for the chaotic regimes $\gamma = 0$ and $\gamma = 0.2$. To interpret the results for the ROM constructed from $\gamma = 5$, we note that all solutions of the gKS equation with $\gamma = 5$ become quasi-periodic in the long term. However, there is a short transient regime ($t \lesssim 5$) during which all solutions exhibit chaotic behavior. Therefore, as W increases, the ratio of these “chaotic” snapshots increases in Φ_{pod} constructed from an FOM applied to the gKS equation with $\gamma = 5$.

Figure 2 also demonstrates that as the number of “chaotic” snapshots in Φ_{pod} increases, ROMs perform better in terms of short-term prediction across all regimes $0 \leq \gamma \leq 10$. Similarly, Figure 3 indicates that ROMs constructed with more “chaotic” snapshots perform better. In particular, in Figure 3, we consider multi-value ROMs, with parameter domains $\hat{\mathcal{G}}_i$ chosen such that the number of “chaotic” snapshots increases with the index i .

4.1.2 Chaotic regime and statistical behavior.

The gKS equation converges to the integrable KdV equation as $\gamma \rightarrow \infty$ and, thus, the long-term behavior of solutions becomes quasi-periodic as γ increases (e.g. [7, 41, 53]). It is possible to identify three different regimes for the long-term behavior of solutions of the gKS equation. Parameter values $\gamma \in [0, 0.19]$ correspond to the chaotic regime, $\gamma \gtrsim 1$ corresponds to quasi-periodic behavior, and $\gamma \in [0.2, 0.9]$ is an intermediate regime where solutions can exhibit transient chaotic behavior for a long time. This behavior of the gKS equation was analyzed extensively numerically in, e.g., [21].

Although, as shown previously, ROM accuracy deteriorates for individual trajectories at times $O(10^2)$, we can compare the long-time statistical behavior of ROMs for the gKS equation. To this end, we compute the power spectra over a long time. The power spectra are given by

$$E_k = \frac{1}{T} \int_0^T |\hat{u}_k(t)|^2 dt,$$

where $\hat{u}_k(t)$ are the coefficients of the Discrete Fourier Transform of the solution $u(x, t)$.

Definition of ROM _{j} with $j = 1, 2, 3$. We consider three particular ROMs discussed previously: ROM₁ is constructed from snapshots computed with $\gamma = 0$, $W = 1$, and $K = 1$; ROM₂ is constructed using $\gamma = 5$, $W = 250$, and $K = 1$; ROM₃ is multi-valued constructed using $K = 5$ and $\hat{\mathcal{G}}_4 = \{0, 0.2, 0.5, 0.7, 0.9\}$.

Figure 4 depicts the power spectra for the FOM and ROM _{j} ($j = 1, 2, 3$), as well as the L^2 error of the individual solution between the FOM and ROM _{j} for $\gamma = 0.1$. Relative L^2 errors are shown on a log-log

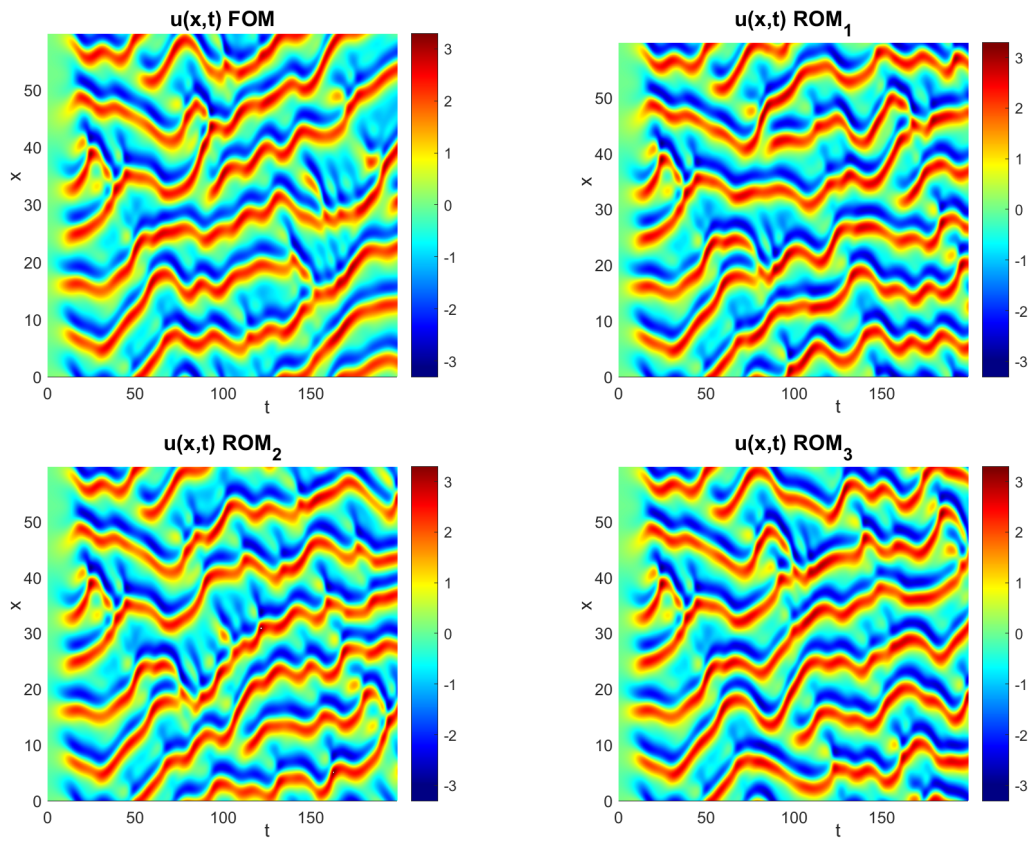


Figure 5: Comparison of an individual solution for FOM and ROM _{j} , $j = 1, 2, 3$, for $\gamma = 0.1$.

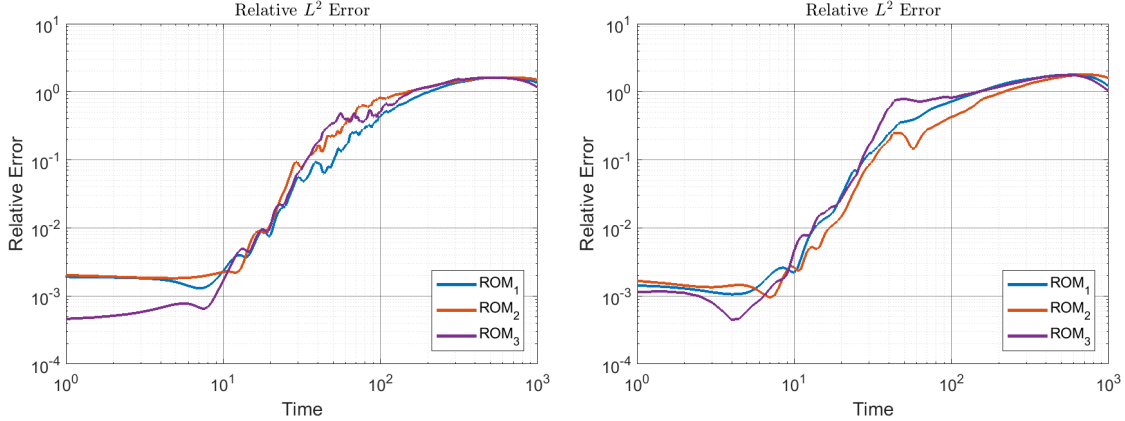


Figure 6: L^2 error for two particular trajectories (given by different initial conditions; left: IC1, right: IC2) in simulations of FOM and ROM_j , $j = 1, 2, 3$ with $\gamma = 0.7$.

scale to emphasize the behavior near $t = 0$ and suppress noisy oscillations in the graph of the relative error. Figure 5 presents a comparison of one particular trajectory on the time interval $[0, 200]$. Numerical solutions computed using the FOM and ROM_j appear very similar for $t \in [0, 80]$. This observation is supported by the Averaged Relative Error depicted in Figure 4.

Larger differences between the numerical solutions computed using the FOM and ROM_j become clearly visible on the time interval $t \in [100, 200]$. However, the statistical behavior remains very similar. Consequently, the power spectra for the FOM and ROM_j (Figure 4) are almost identical for low wavenumbers, with only a small discrepancy observed at higher wavenumbers in the ROM_j simulations.

All three ROMs successfully reproduce the solution on the time interval $[0, 80]$ (short-term prediction) and correctly capture the statistical behavior of the solutions for longer times. This outcome is expected since the gKS equation exhibits chaotic solutions for $\gamma = 0.1$, and numerical errors eventually lead to rapidly divergent trajectories of the ROM and FOM solutions. Nevertheless, all three ROMs accurately capture the behavior of the attractor of the gKS equation.

4.1.3 Transient regime and persistent patterns.

For $\gamma > 0.2$, statistical properties of the gKS equation become dependent on the initial condition. Therefore, we do not present the averaged power spectra for values of $\gamma > 0.2$. For $\gamma \in [0.2, 0.9]$, solutions can exhibit long chaotic-like transition periods, but eventually, solutions become quasi-periodic and persistent patterns emerge.

We present the results of ROM and FOM numerical simulations for $\gamma = 0.7$ and two particular initial conditions (IC1 and IC2) in Figures 6, 7, and 8. For both initial conditions, the solutions demonstrate persistent traveling wave-like structures that form beyond the transient stage at longer times. The speed, width, and amplitude of these traveling structures are clearly dependent on the initial conditions.

We observe that all three ROMs accurately reproduce the solution up to $t \simeq 10$, after which the relative L^2 error between the ROM and FOM solutions begins to grow, reaching $O(1)$ around $t = 100$; see Figure 6. Nevertheless, the persistent solution patterns are very well reproduced by the ROMs when the long-term behavior of solutions is of interest. The larger errors for $t > 100$ can be attributed to small phase shifts in the traveling-wave solutions between the ROMs and the FOMs.

We conclude that the error norm, a commonly used statistic for assessing the quality of a ROM, may be inadequate for systems that exhibit laminar solutions with persistent patterns emerging after a transition stage.

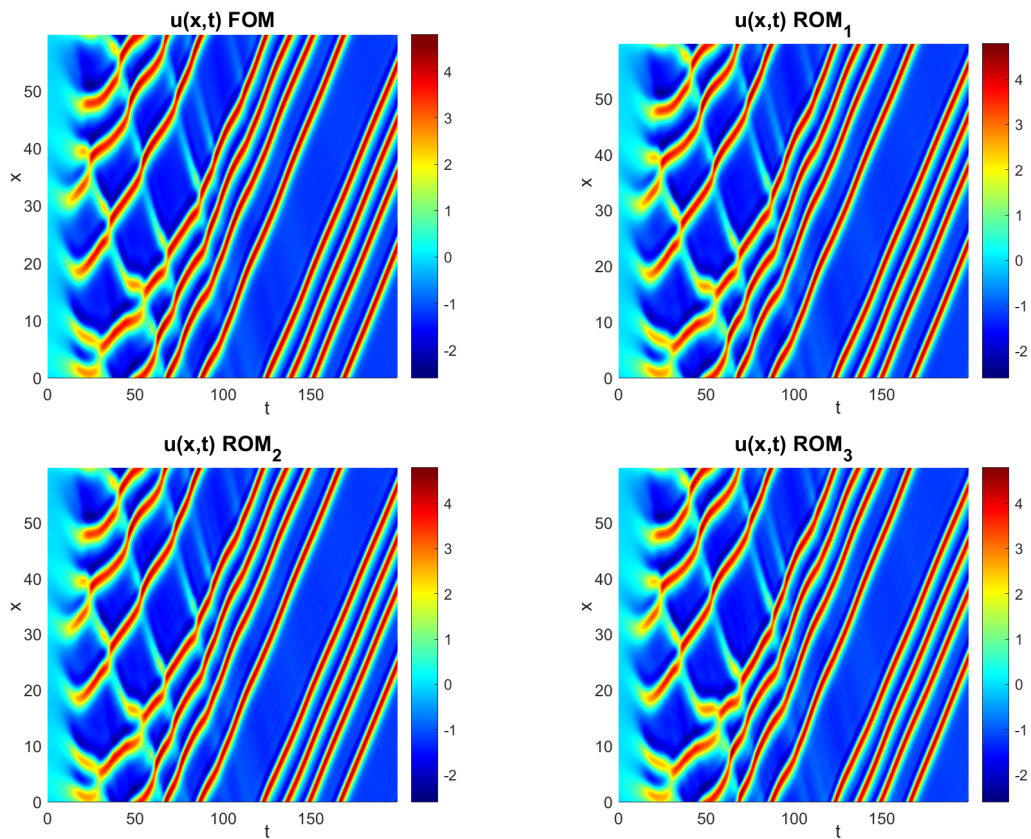


Figure 7: Snapshots for solutions in simulations of FOM and ROM _{j} , $j = 1, 2, 3$ with $\gamma = 0.7$. Initial condition IC1.

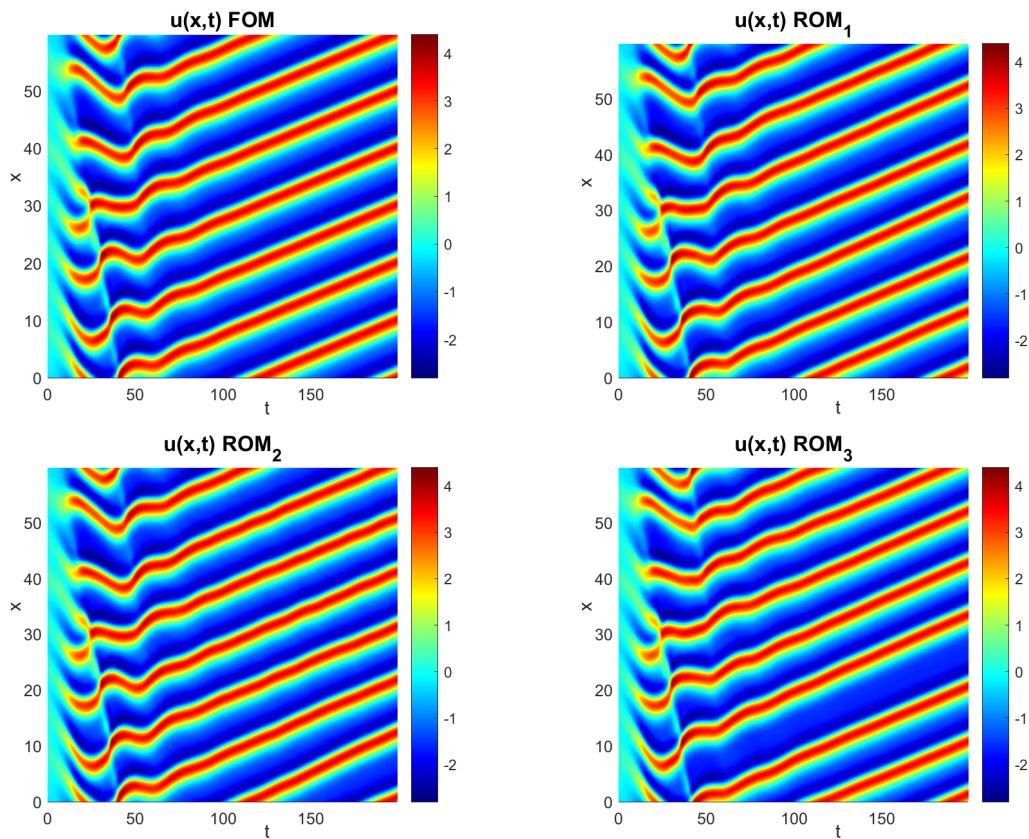


Figure 8: Snapshots for solutions in simulations of FOM and ROM _{j} , $j = 1, 2, 3$ with $\gamma = 0.7$. Initial condition IC2.

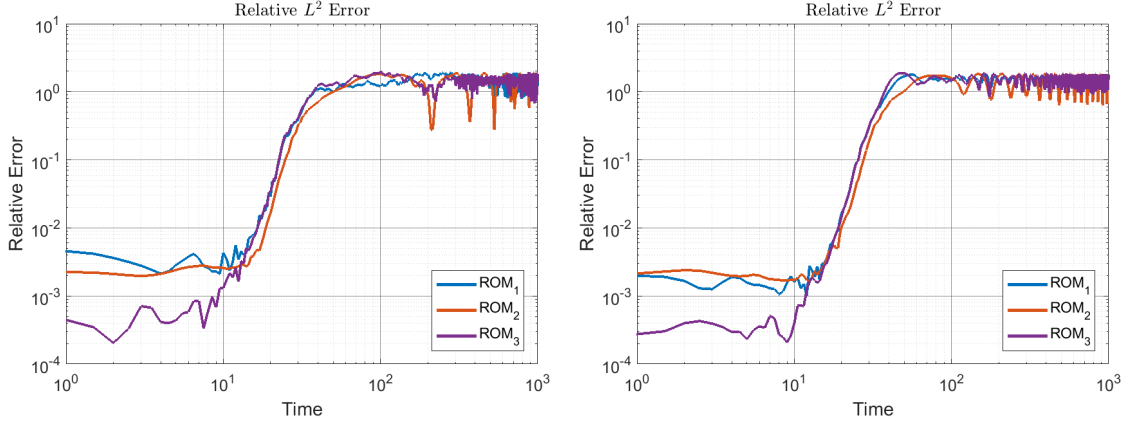


Figure 9: L^2 error for two particular trajectories (given by different initial conditions; left: IC1, right: IC2) in simulations of FOM and ROM_j , $j = 1, 2, 3$ with $\gamma = 3$.

4.1.4 Laminar regime and quasi-periodic solutions.

For larger γ the gKS system becomes deterministic with solutions exhibiting a short transition period before reaching a quasi-periodic state. Both the transition period and the quasi-periodic state are initial condition dependent. The later makes it hard to predict long term solution behavior especially if the initial condition is not within (or very close to) the training set of initial conditions. This phenomenon is illustrated by the following example of recovering gKS solution for $\gamma = 3$.

Figures 9–10 show the results of ROM_j , $j = 1, 2, 3$, and FOM numerical simulations for $\gamma = 3$ and two particular initial conditions (IC1 and IC2). All three ROMs accurately reproduce the solution up to $t \simeq 10$, after which the relative L^2 error between the ROM and FOM solutions begins to grow, reaching $O(1)$ around $t = 40$; see Figure 9. Unlike the transitional case with persistent solution patterns, the ROMs fail to accurately reproduce the quasi-periodic state of the solution. However, we observe that ROM_2 performs somewhat better in the long term, offering the best recovery of the quasi-periodic states among all ROMs considered.

We note that other variants of ROMs described at the beginning of the section were also applied in this example. In particular, variants of multi-parameter ROMs with training sets $\widehat{\mathcal{G}}_i$, $i = 1, 2, 3$, were tested. They all demonstrated results no better than ROM_1 or ROM_3 . Notably, the results for the multi-parameter ROM with training set $\widehat{\mathcal{G}}_1$ were the least accurate, despite $\gamma = 3$ being among the training values for this ROM. We omit presenting these results for brevity. A similar pattern was observed when ROM and FOM solutions were compared for gKS with $\gamma = 5$.

4.2 POD-DEIM and POD ROM comparison

A hyper-reduction technique is generally required for effective handling of non-linear terms in a projection-based ROM. In this final set of experiments, we demonstrate that applying the discrete empirical interpolation method (DEIM) leads to a reduced model that is as accurate as the (computationally expensive) true projection. In other words, we compare ROMs given by (6) and (11).

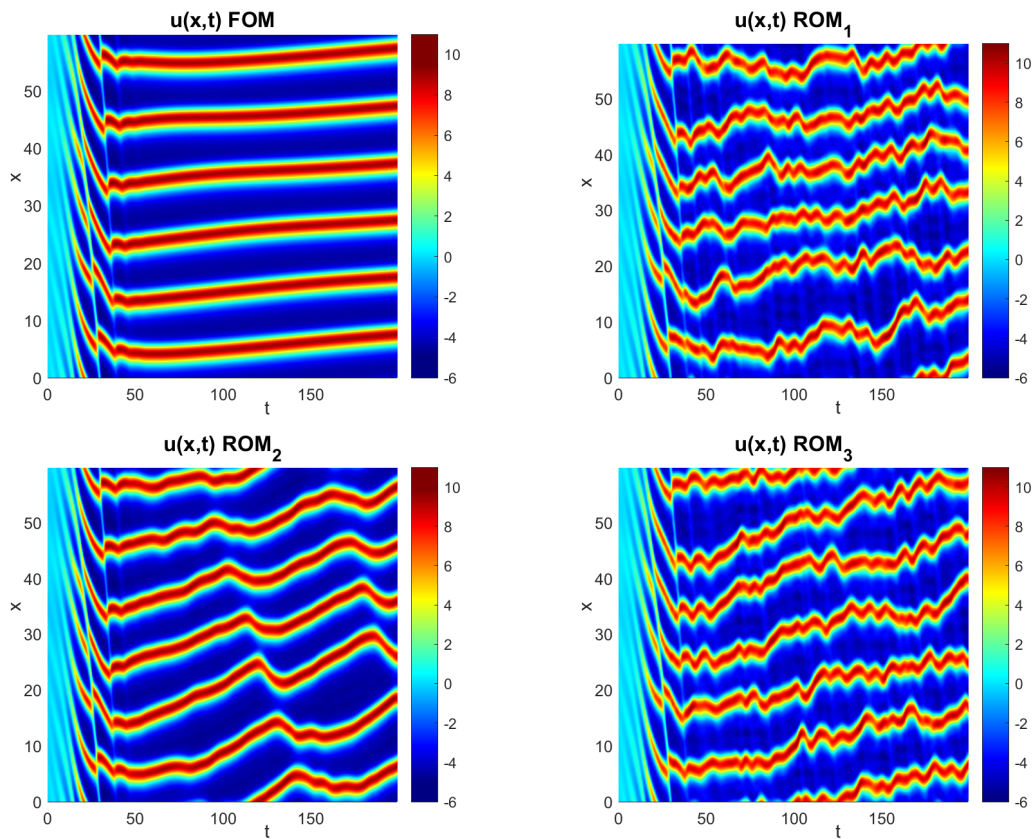


Figure 10: Snapshots for solutions in simulations of FOM and ROM_j , $j = 1, 2, 3$ with $\gamma = 3$. Initial condition IC1. ROM_3 is constructed with $\widehat{\mathcal{G}}_4 = \{0, 0.2, 0.5, 0.7, 0.9\}$.

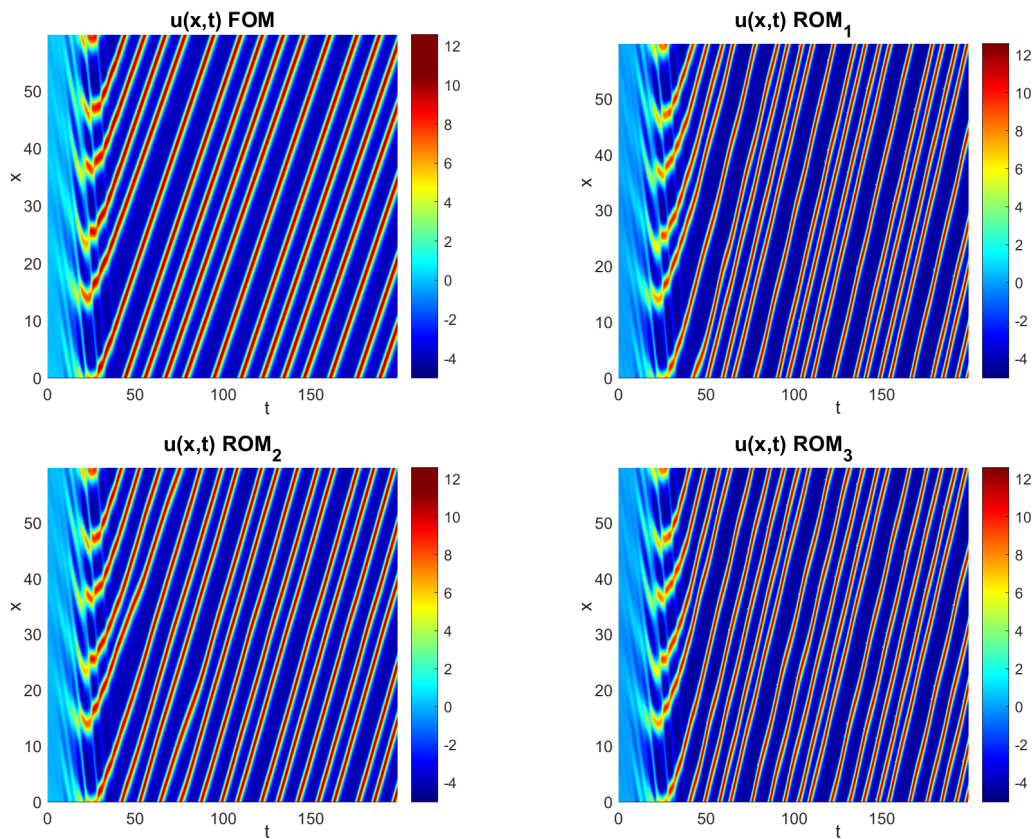


Figure 11: Snapshots for solutions in simulations of FOM and ROM_j , $j = 1, 2, 3$ with $\gamma = 3$. Initial condition IC2. ROM_3 is constructed with $\hat{\mathcal{G}}_4 = \{0, 0.2, 0.5, 0.7, 0.9\}$.

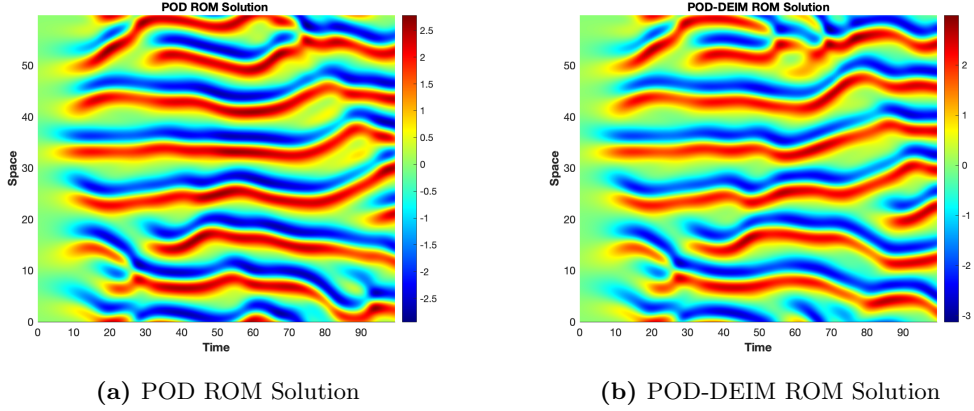


Figure 12: POD-DEIM ROM vs POD ROM for $\gamma = 0$.

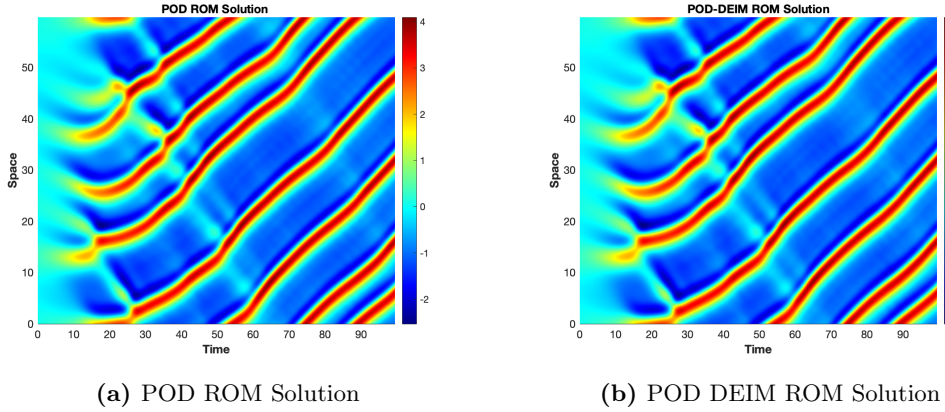


Figure 13: POD-DEIM ROM vs POD ROM for $\gamma = 0.5$.

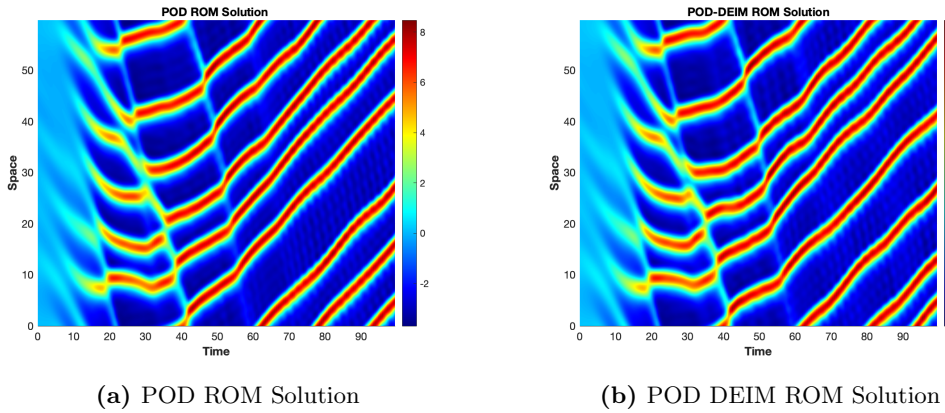


Figure 14: POD-DEIM ROM vs POD ROM for $\gamma = 2$.

Figures 12–14 present results with POD–DEIM and POD ROMs applied to predict solutions of the KS and gKS equations for $\gamma = 0, 0.5$, and 2 . We show the results only for the single-valued ROM built from $\gamma = 0$

snapshots, as the results for ROMs built from other snapshot collections were also almost indistinguishable between the POD–DEIM and POD variants.

5 Conclusions

For the example of the KS and gKS equations, we investigated the ability of parametric POD-ROMs to predict solutions over a range of parameters that include various regimes exhibited by the KS and gKS solutions: chaotic, transitional, and quasi-periodic dynamics. Several single-parameter and multi-parameter training strategies were applied to train the reduced-order model. We found that efficient prediction of solutions beyond the set of parameters and initial conditions used to generate the training data requires including more snapshots that represent chaotic or short-time transient behaviors of the gKS model.

The results suggest that POD-ROM is capable of reproducing statistical properties of turbulent solutions, such as power spectra, and accurately recovers the solution over relatively short time intervals. This prediction time depends on the chosen training strategy. For the transitional regime, characterized by an initial period of (quasi-)chaotic behavior followed by a more laminar regime, a properly trained POD-ROM can recover persistent patterns of the laminar solution. These patterns emerge in the ROM solution with a phase shift. We conclude that for such systems, simply computing the norm of the error between FOM and ROM solutions may not be a sufficient assessment of ROM quality.

The quasi-periodic regimes proved to be the most resistant to effective POD-ROM simulations when initial conditions and parameter values were not included in the training sets. Interestingly, ROMs trained with more data from chaotic and transitional regimes yielded somewhat better results in these cases. Developing more universal projection-based ROMs that perform equally well across all regimes—from turbulent to laminar—may require employing parameter-specific ROM bases, potentially exploiting ideas of tensor-based ROMs. We plan to explore this research direction in future work.

Acknowledgment

The authors R.B.M. and M.O. were supported in part by the U.S. National Science Foundation under awards DMS-2309197 and DMS-2408978.

A Initial Conditions

Initial conditions in the simulations of the KS and the gKS equation are given by (12).

Initial conditions for Figure 5 were generated with $J = 8$ using $A_j = \{3.0233, 3.5171, -7.3354, -9.6221, -1.9993, 5.3954, -6.7118, -4.5122\} \times 10^{-2}$ and $\phi_j = \{6.08, 3.0139, 6.2266, 3.1967, 4.983, 3.0123, 3.6808, 2.2941\}$.

IC1 and IC2 in this paper were generated with $J = 8$. Specific values of coefficients and phases for IC1 are $A_j^{(1)} = \{0.1593, -8.4911, 5.6365, 5.4644, -1.8904, 6.2566, 1.7180, -2.1826\} \times 10^{-2}$ and $\phi_j^{(1)} = \{3.5963, 2.1939, 4.1857, 5.4722, 5.5467, 4.5229, 1.2151, 0.16661\}$. Values of these parameters for IC2 are $A_j^{(2)} = \{-1.5013, 7.649, 1.891, 8.5255, 5.531, 2.4718, 6.5647, 9.6781\} \times 10^{-2}$ and $\phi_j^{(2)} = \{3.3396, 3.6174, 1.7775, 5.3945, 2.7183, 0.1965, 5.1264, 4.5449\}$.

References

- [1] M. ABADIE, P. BECK, J. P. PARKER, AND T. M. SCHNEIDER, *The topology of a chaotic attractor in the kuramoto-sivashinsky equation*, arXiv preprint arXiv:2409.01719, (2024).
- [2] D. AMSALLEM AND C. FARHAT, *Interpolation method for adapting reduced-order models and application to aeroelasticity*, AIAA journal, 46 (2008), pp. 1803–1813.

- [3] D. AMSALLEM, M. J. ZAHR, AND C. FARHAT, *Nonlinear model order reduction based on local reduced-order bases*, International Journal for Numerical Methods in Engineering, 92 (2012), pp. 891–916.
- [4] N. BALMFORTH, *Solitary waves and homoclinic orbits*, Annual review of fluid mechanics, 27 (1995), pp. 335–373.
- [5] P. BENNER, S. GUGERCIN, AND K. WILLCOX, *A survey of projection-based model reduction methods for parametric dynamical systems*, SIAM review, 57 (2015), pp. 483–531.
- [6] H.-C. CHANG, E. DEMEKHIN, AND E. KALAININ, *Interaction dynamics of solitary waves on a falling film*, Journal of Fluid Mechanics, 294 (1995), pp. 123–154.
- [7] H.-C. CHANG, E. A. DEMEKHIN, AND D. I. KOPELEVICH, *Laminarizing effects of dispersion in an active-dissipative nonlinear medium*, Physica D: Nonlinear Phenomena, 63 (1993), pp. 299–320.
- [8] S. CHATURANTABUT AND D. C. SORENSEN, *Nonlinear model reduction via discrete empirical interpolation*, SIAM Journal on Scientific Computing, 32 (2010), pp. 2737–2764.
- [9] F. CHINESTA, A. AMMAR, AND E. CUETO, *Recent advances and new challenges in the use of the proper generalized decomposition for solving multidimensional models*, Archives of Computational methods in Engineering, 17 (2010), pp. 327–350.
- [10] F. CHINESTA, R. KEUNINGS, AND A. LEYGUE, *The proper generalized decomposition for advanced numerical simulations: a primer*, Springer Science & Business Media, 2013.
- [11] P. COLLET, J.-P. ECKMANN, H. EPSTEIN, AND J. STUBBE, *Analyticity for the Kuramoto-Sivashinsky equation*, Physica D: Nonlinear Phenomena, 67 (1993), pp. 321–326.
- [12] P. CONSTANTIN, C. FOIAS, B. NICOLAENKO, AND R. TEMAM, *Integral manifolds and inertial manifolds for dissipative partial differential equations*, vol. 70, Springer Science & Business Media, 2012.
- [13] C. DUPRAT, F. GIORGIUTTI-DAUPHINÉ, D. TSELUIKO, S. SAPRYKIN, AND S. KALLIADASIS, *Liquid film coating a fiber as a model system for the formation of bound states in active dispersive-dissipative nonlinear media*, Physical review letters, 103 (2009), p. 234501.
- [14] C. DUPRAT, D. TSELUIKO, S. SAPRYKIN, S. KALLIADASIS, AND F. GIORGIUTTI-DAUPHINÉ, *Wave interactions on a viscous film coating a vertical fibre: Formation of bound states*, Chemical Engineering and Processing: Process Intensification, 50 (2011), pp. 519–524.
- [15] J. L. EFTANG, D. J. KNEZEVIC, AND A. T. PATERA, *An hp certified reduced basis method for parametrized parabolic partial differential equations*, Mathematical and Computer Modelling of Dynamical Systems, 17 (2011), pp. 395–422.
- [16] J. L. EFTANG, A. T. PATERA, AND E. M. RØNQUIST, *An “hp” certified reduced basis method for parametrized elliptic partial differential equations*, SIAM Journal on Scientific Computing, 32 (2010), pp. 3170–3200.
- [17] S.-I. EI AND T. OHTA, *Equation of motion for interacting pulses*, Physical Review E, 50 (1994), p. 4672.
- [18] C. FARIÁS, C. BAYONA-ROA, E. CASTILLO, R. C. CABRALES, AND R. REYES, *Reduced order modeling of parametrized pulsatile blood flows: Hematocrit percentage and heart rate*, International Journal of Engineering Science, 193 (2023), p. 103943.
- [19] H. FISCHER, A. FAU, AND T. WICK, *Reduced-order modeling for parametrized time-dependent Navier–Stokes equations*, PAMM, 23 (2023), p. e202200265.

- [20] C. FOIAS, B. NICOLAENKO, G. SELL, AND R. TEMAM, *Inertial manifolds for the Kuramoto-Sivashinsky equation and an estimate of their lowest dimension*, Journal de Mathématiques Pures et Appliquées, 67 (1988), pp. 197–226.
- [21] H. GOTODA, M. PRADAS, AND S. KALLIADASIS, *Nonlinear forecasting of the generalized Kuramoto-Sivashinsky equation*, International Journal of Bifurcation and Chaos, 25 (2015), p. 1530015.
- [22] M. W. HESS, A. QUAINI, AND G. ROZZA, *A data-driven surrogate modeling approach for time-dependent incompressible Navier-Stokes equations with dynamic mode decomposition and manifold interpolation*, Advances in Computational Mathematics, 49 (2023), p. 22.
- [23] J. M. HYMAN, B. NICOLAENKO, AND S. ZALESKI, *Order and complexity in the Kuramoto-Sivashinsky model of weakly turbulent interfaces*, Physica D: Nonlinear Phenomena, 23 (1986), pp. 265–292.
- [24] M. S. JOLLY, I. G. KEVREKIDIS, AND E. S. TITI, *Approximate inertial manifolds for the Kuramoto-Sivashinsky equation: analysis and computations*, Physica D: Nonlinear Phenomena, 44 (1990), pp. 38–60.
- [25] S. KALLIADASIS, C. RUYER-QUIL, B. SCHEID, AND M. G. VELARDE, *Falling liquid films*, vol. 176, Springer Science & Business Media, 2011.
- [26] E. N. KARATZAS, M. NONINO, F. BALLARIN, AND G. ROZZA, *A reduced order cut finite element method for geometrically parametrized steady and unsteady Navier-Stokes problems*, Computers & Mathematics with Applications, 116 (2022), pp. 140–160.
- [27] T. KAWAHARA, *Formation of saturated solitons in a nonlinear dispersive system with instability and dissipation*, Physical review letters, 51 (1983), p. 381.
- [28] I. G. KEVREKIDIS, B. NICOLAENKO, AND J. C. SCOVEL, *Back in the saddle again: a computer assisted study of the Kuramoto-Sivashinsky equation*, SIAM Journal on Applied Mathematics, 50 (1990), pp. 760–790.
- [29] Y. KURAMOTO AND T. TSUZUKI, *Persistent propagation of concentration waves in dissipative media far from thermal equilibrium*, Progress of theoretical physics, 55 (1976), pp. 356–369.
- [30] C. LEE AND H. TRAN, *Reduced-order-based feedback control of the kuramoto-sivashinsky equation*, Journal of computational and applied mathematics, 173 (2005), pp. 1–19.
- [31] F. LU, K. K. LIN, AND A. J. CHORIN, *Data-based stochastic model reduction for the kuramoto-sivashinsky equation*, Physica D: Nonlinear Phenomena, 340 (2017), pp. 46–57.
- [32] J. L. LUMLEY, *The structure of inhomogeneous turbulent flows*, Atmospheric turbulence and radio wave propagation, (1967).
- [33] A. J. MAJDA AND I. TIMOFEYEV, *Remarkable statistical behavior for truncated Burgers-Hopf dynamics*, 97 (2000), pp. 12413–12417.
- [34] A. V. MAMONOV AND M. A. OLSHANSKII, *Interpolatory tensorial reduced order models for parametric dynamical systems*, Computer Methods in Applied Mechanics and Engineering, 397 (2022), p. 115122.
- [35] ———, *Tensorial parametric model order reduction of nonlinear dynamical systems*, SIAM Journal on Scientific Computing, 46 (2024), pp. A1850–A1878.
- [36] P. MANNEVILLE, *Liapounov exponents for the kuramoto-sivashinsky model*, in Macroscopic Modelling of Turbulent Flows: Proceedings of a Workshop Held at INRIA, Sophia-Antipolis, France, December 10–14, 1984, Springer, 1985, pp. 319–326.

- [37] E. MENIER, M. A. BUCCI, M. YAGOUBI, L. MATHELIN, AND M. SCHOENAUER, *Cd-rom: Complemented deep-reduced order model*, Computer Methods in Applied Mechanics and Engineering, 410 (2023), p. 115985.
- [38] M. MÜNDEL AND F. KAISER, *An intermittency route to chaos via attractor merging in the Laser-Kuramoto-Sivashinsky equation*, Physica D: Nonlinear Phenomena, 98 (1996), pp. 156–170.
- [39] B. NICOLAENKO, B. SCHEURER, AND R. TEMAM, *Some global dynamical properties of the Kuramoto-Sivashinsky equations: nonlinear stability and attractors*, Physica D: Nonlinear Phenomena, 16 (1985), pp. 155–183.
- [40] F. PICHI, F. BALLARIN, G. ROZZA, AND J. S. HESTHAVEN, *An artificial neural network approach to bifurcating phenomena in computational fluid dynamics*, Computers & Fluids, 254 (2023), p. 105813.
- [41] M. PRADAS, D. TSELUIKO, AND S. KALLIADASIS, *Rigorous coherent-structure theory for falling liquid films: Viscous dispersion effects on bound-state formation and self-organization*, Physics of Fluids, 23 (2011).
- [42] R. REYES, O. RUZ, C. BAYONA-ROA, E. CASTILLO, AND A. TELLO, *Reduced order modeling for parametrized generalized Newtonian fluid flows*, Journal of Computational Physics, 484 (2023), p. 112086.
- [43] C. W. ROWLEY, *Model reduction for fluids, using balanced proper orthogonal decomposition*, International Journal of Bifurcation and Chaos, 15 (2005), pp. 997–1013.
- [44] M. SCHMUCK, M. PRADAS, G. A. PAVLIOTIS, AND S. KALLIADASIS, *A new mode reduction strategy for the generalized kuramoto-sivashinsky equation*, IMA Journal of Applied Mathematics, 80 (2015), pp. 273–301.
- [45] D. SIPP, M. F. DE PANDO, AND P. J. SCHMID, *Nonlinear model reduction: a comparison between pod-galerkin and pod-deim methods*, Computers & Fluids, 208 (2020), p. 104628.
- [46] L. SIROVICH, *Turbulence and the dynamics of coherent structures. i. coherent structures*, Quarterly of applied mathematics, 45 (1987), pp. 561–571.
- [47] G. SIVASHINSKY, *Nonlinear analysis of hydrodynamic instability in laminar flames—I. Derivation of basic equations*, Acta Astronautica, 4 (1977), pp. 1177–1206.
- [48] Y. S. SMYRLIS AND D. T. PAPAGEORGIOU, *Predicting chaos for infinite dimensional dynamical systems: the Kuramoto-Sivashinsky equation, a case study*, Proceedings of the National Academy of Sciences, 88 (1991), pp. 11129–11132.
- [49] N. T. SON, *A real time procedure for affinely dependent parametric model order reduction using interpolation on grassmann manifolds*, International Journal for Numerical Methods in Engineering, 93 (2013), pp. 818–833.
- [50] P. STINIS, *Stochastic optimal prediction for the kuramoto-sivashinsky equation*, Multiscale Modeling & Simulation, 2 (2004), pp. 580–612.
- [51] R. TEMAM, *Infinite-dimensional dynamical systems in mechanics and physics*, vol. 68, Springer Science & Business Media, 2012.
- [52] R. TEMAM AND X. M. WANG, *Estimates on the lowest dimension of inertial manifolds for the Kuramoto-Sivashinsky equation in the general case*, Differential Integral Equations, 7 (1994), pp. 1095–1108.
- [53] D. TSELUIKO AND S. KALLIADASIS, *Weak interaction of solitary pulses in active dispersive-dissipative nonlinear media*, The IMA Journal of Applied Mathematics, 79 (2014), pp. 274–299.

- [54] D. TSELUIKO, S. SAPRYKIN, AND S. KALLIADASIS, *Coherent structures theory for the generalized kuramoto-sivashinsky equation*, Journal of Physics: Conference Series, 216 (2010), p. 012018.
- [55] N. J. ZABUSKY AND M. D. KRUSKAL, *Interaction of "solitons" in a collisionless plasma and the recurrence of initial states*, Physical review letters, 15 (1965), p. 240.
- [56] X. ZHANG, P. ZHANG, AND Y. DING, *A reduced high-order compact finite difference scheme based on proper orthogonal decomposition for the generalized kuramoto-sivashinsky equation*, IAENG International Journal of Applied Mathematics, 49 (2019), pp. 1–10.